ADVANCED SUSTAINABLE SYSTEMS
www.advsustainsys.com

Ni Surface & Polyacryloyl Hydrazide Mediated Growth of Co_3O_4@NiCu Alloy Nanocuboids for Effective Methanol Oxidation and Oxygen Evolution Reactions

*Santosh Semwal, Aiswarya Samal, Saroj Kumar Nayak, Rajashri R. Urkude, Akhoury Sudhir Kumar Sinha, and Umaprasana Ojha**

Strategies to control the size, shape, and lattice arrangement, introduce doping agents, and induce heterostructuring in electrocatalysts are strongly desirable to tailor their activities. Herewith, a one-pot strategy utilizing polyacryloyl hydrazide (PAHz) as the composition directing agent and metallic Ni surface as the shape directing agent is employed to grow Co_3O_4 doped NiCu alloy nanocuboids on Ni foam (NF) under hydrothermal conditions for electrocatalytic H_2 production. The resulting bi-functional electrodes are suitable for methanol oxidation reaction (MOR) coupled green H_2 production with effective energy efficiency. The low overall potential (MOR+HER) of 1.78 V to realize the current density (*j*) value of 100 mA cm^{-2} and extended durability (100 h@10 mA cm^{-2}) along with the selective conversion of methanol to formate support the viability of the NF-PAHz-Co_3O_4@NiCu for the said operation. The electrode also displays efficacy toward oxygen evolution reaction (OER) activity and j_{OER} value of 100 mA cm^{-2} is realized at a potential value of 1.65 V_{RHE} with adequate durability. Overall, the synthetic strategy is general, scalable and may be extended to grow other metal oxide doped alloy nanostructures in the future.

1. Introduction

Electrocatalysis plays an essential role in production and utilization of certain clean energy resources and effective utilization of greenhouse gases.[1,2] Production of green hydrogen (H_2) is one of the prominent avenue, where electrocatalysis constitutes the core reaction for splitting of water to H_2 and O_2.[3,4] A number of half-cell reactions are studied in recent literature to enhance the overall energy efficiency of the process, which is one of the prominent concerns obstructing the commercial viability of the technology.[5,6] Among the various half-cell reactions explored in literature to improve the energy efficiency of the water splitting process, methanol oxidation reaction (MOR) is significant owing to its low theoretical onset potential and viable side products.[7,8] Therefore, MOR coupled hydrogen evolution reaction (HER) offers a plausible avenue to produce clean H_2 energy in an affordable manner satisfying one of the United Nations sustainable development goals. A number of electrocatalysts possessing adequate catalytic efficiency toward MOR are developed and studied in recent literature.[9,10] For example, periodically assembled Pt–Au hetero nanostructures exhibited superior MOR activity compared to that of the Pt/C in 0.1 M $HClO_4$ solution.[11] Alloying of CoPt catalyst with Mn improved both the activity and durability of MOR in acidic media.[12] Especially, nanostructures based on transition metal alloys have displayed proficiency toward various electrochemical reactions in literature.[13,14] For example, CoNi alloy/CoNi layered double hydroxide activated MoS_2 nanosheets displayed effective H_2 evolution activity under basic conditions.[15] Among the active catalytic systems, NiCu alloy-based nanocatalysts have exhibited effective MOR coupled water splitting activities under different pH conditions.[16,17] For example, Cu/NiCu nanowires synthesized using a two-step procedure produced a mass j_{MOR} value of 867.1 mA mg$-^1{}_{metal}$ at 1.55 V_{RHE}.[18] Similarly, NiCu@C nanoparticles-based system produced mass j_{MOR} value of 1028 mA/mg$-^1{}_{metal}$ at 1.55 V_{RHE} under alkaline conditions.[19] Though, the results were promising, further improvement in *j* value at low potential is desirable to exploit the system for commercial utilization.

S. Semwal, U. Ojha
Department of Sciences & Humanities
Rajiv Gandhi Institute of Petroleum Technology
Jais, Uttar Pradesh 229304, India
E-mail: uojha@iitbbs.ac.in

A. Samal, S. K. Nayak, U. Ojha
School of Basic Sciences
Indian Institute of Technology
Jatni, Bhubaneswar, Odisha 752050, India

R. R. Urkude
Beamline Development and Application Section
Bhabha Atomic Research Center
Trombay, Mumbai 400085, India

A. S. K. Sinha
Department of Chemical Engineering
Rajiv Gandhi Institute of Petroleum Technology
Jais, Uttar Pradesh 229304, India

The ORCID identification number(s) for the author(s) of this article can be found under https://doi.org/10.1002/adsu.202400372

DOI: 10.1002/adsu.202400372

Recently, polymer-based metal nanoparticles have emerged as an interesting class of electrocatalysts, as they combine the advantages of both polymeric supports and nanoscale metals.[20,21] The polymer matrix offers stability, chemical resistance, and a tunable environment for controlling the nanoparticle morphology, while the metal nanoparticles serve as the active sites for effective catalytic actions.[22,23] Polymeric coatings based on their hydrophobicity/ hydrophilicity and surface charges are also known to tune the surface electronic properties of the catalyst.[24] Recently, various polymer-based metal nanocomposites have been explored based on earth-abundant metals and conducting polymers or carbon-based supports.[25,26] Importantly, metal-polymer nanocomposites are primed to serve as catalysts for sustainable H_2 production from various water sources.[27] For example, CoO_x nanoparticles dispersed in poly(pyrrole-alkylammonium) system exhibited effective oxygen evolution reaction (OER) activity under alkaline conditions.[28]

Nickel foam (NF) is a porous material with high electronic conductivity, durability in alkaline solutions, and an appropriate structure for releasing gas bubbles. In this approach, three aspects, i.e., metallic oxide doping, shape orientation of nanostructures, and enhancement of surface area are targeted in a one-pot synthetic procedure to grow bimetallic alloy nanostructure on NF for MOR application. Especially, to grow alloy or multi-metallic nanostructures of a particular shape and size is advantageous, since the shape of nanocatalyst is known to control the activity.[29] The possibility to dope the above alloy nanostructures with oxides is targeted to promote the activity further as metal oxide doping is known to alter the electronic structure leading to bandgap optimization necessary for tailoring of catalytic activity.[30] Furthermore, the role of active metal surface as a shape-directing agent toward the growth of bimetallic nanostructures is not well explored in literature to the best of our knowledge. Additionally, the composition-directing ability of a polymeric reductant is also included in the design to develop a nanocatalyst system with adequate activity and sustainability.

Herewith, polyacryloyl hydrazide (PAHz) as the reducing and capping agent is utilized to in situ grow NiCu alloy nanostructures from their salts under hydrothermal conditions.[31] In literature, PAHz is already known to effectively reduce various metal salts to the corresponding nanoparticle in aqueous solution.[32–34] PAHz was utilized to synthesize size-controlled Ag and Au nanoparticles in aqueous solutions under ambient conditions.[35] A carbonyl hydrazide functionalized star polymer was employed to swiftly convert various precious metal ions to the corresponding nanoparticles in solution.[36] Similarly, membranes based on carbon nanotube (CNT) modified with PAHz were utilized to separate various metal ions from oil-water emulsion through the formation of corresponding nanoparticles.[37] In this approach, the potential selective reducing ability of PAHz toward various metal ions is utilized to synthesize a metal oxide doped nanoalloy for utilization toward electrocatalysis. Furthermore, the possible role of NF surface as the nucleating site to direct the shape of the above nanostructure is also explored.[38,39] Overall, a one-pot strategy is designed to grow PAHz capped Co_3O_4@NiCu alloy nanocrystals on NF for utilization as active electrodes for MOR and OER activities in an alkaline medium. We focus on investigating the impacts of material synthesis, nanocatalyst composition, and electrode structure to optimize MOR and OER performances under membrane-less conditions. Through detailed electrochemical analysis paired with physical and morphological characterization, we demonstrate the catalytic efficacy and stability of the developed electrodes in alkaline media compared to that of the state-of-the-art benchmark electrocatalysts. Overall, this work provides critical insights into the design principles for polymer-based nanocomposite catalysts toward realizing their potential for efficient and durable alkaline water splitting and MOR.

2. Results and Discussion

$Cu(NO_3)_2.3H_2O$ and $Co(NO_3)_2.6H_2O$ in equimolar proportions were taken in PAHz aqueous solution possessing an NF piece and subjected to hydrothermal treatment at 120 °C to synthesize the NF-PAHz-Co_3O_4@NiCu alloy nanocuboids (**Scheme 1**). NF served as the Ni source to facilitate the formation of the above alloy nanocuboids under hydrothermal conditions as similarly reported in literature for other systems.[40–42] Control samples devoid of NF (PAHz-Cu) and Co^{2+} (NF-PAHz-NiCu) were also synthesized to understand the growth mechanism. The X-ray diffraction (XRD) trace of NF-PAHz-Co_3O_4@NiCu displayed 2θ peaks at 43.41°, 50.56°, and 74.20° accountable to 111, 200, and 220 planes of Cu(0), respectively (**Figure 1A**). The 2θ value corresponding to 111 shifted by 0.12° compared to that of the Cu(0)-JCPDS suggesting possible formation of NiCu alloy (Figure 1B).[43] The peaks at 36.59°, 38.49°, and 59.03° assigned to the 311, 222, and 511 planes respectively of Co_3O_4 dopant were visible in the XRD trace. The peaks accountable to Ni(0) and the NF appeared at 44.51 (111), 51.86 (200), and 76.38° (220) (Figure 1A). The XRD data of the control (NF-PAHz-NiCu) synthesized in the absence of Co^{2+} revealed 2θ peaks corresponding to Cu(0) and Ni(0) in positions similar to that of the NF-PAHz-Co_3O_4@NiCu supporting the formation of NiCu alloy (Figure S1, Supporting Information). However, the sample (PAHz-Cu) synthesized in the absence of NF displayed 2θ peaks corresponding to Cu(0) only and no peaks accountable to the Co_3O_4 and Ni(0) were visible suggesting the formation of PAHz-Cu composite and possible inability of Ni^{2+} and Co^{2+} to participate in the nanoparticle formation (Figure S2, Supporting Information).

The Cu 2p X-ray photoelectron spectroscopy (XPS) data displayed a pair of peaks at 932.7 and 952.5 eV suggesting the presence of Cu(0) in the NF-PAHz-Co_3O_4@NiCu (Figure 1C).[44] A minor peak at 934.3 eV accountable to the oxidized form (CuO) was also visible in spectra. Importantly, the oxidized peak was relatively small and Cu(0) is known to oxidize in air during the characterization process.[45] The Ni 2p XPS data revealed the presence of peaks at 852.8 and 870.1 eV accountable to the Ni(0) present in the NF-PAHz-Co_3O_4@NiCu (Figure 1D). Furthermore, the Cu 2p (−0.30 eV) and Ni 2p (0.17 eV) peaks displayed minor shifts in peak position compared to that of the pure single metal system supporting the alloy formation.[42,26] The Co 2p XPS spectra displayed prominent peaks at 781.8 and 779.3 eV suggesting the presence of Co^{2+} and Co^{3+} respectively in Co_3O_4 (Figure 1E).[46] The O 1s peak at 531.2 eV supported the presence of Co_3O_4 in the sample.[47] The N 1s peaks at 399.0 (NH) and 400.1 eV (C–N), the C 1s peaks at 284.8 (C–C), 286.4 (C–N), and 288.3 eV (C═O) and O 1s peak at 532.8 eV (C═O) supported the presence of PAHz in the sample (Figure 1F; Figure S3, Supporting Information).[48–50]

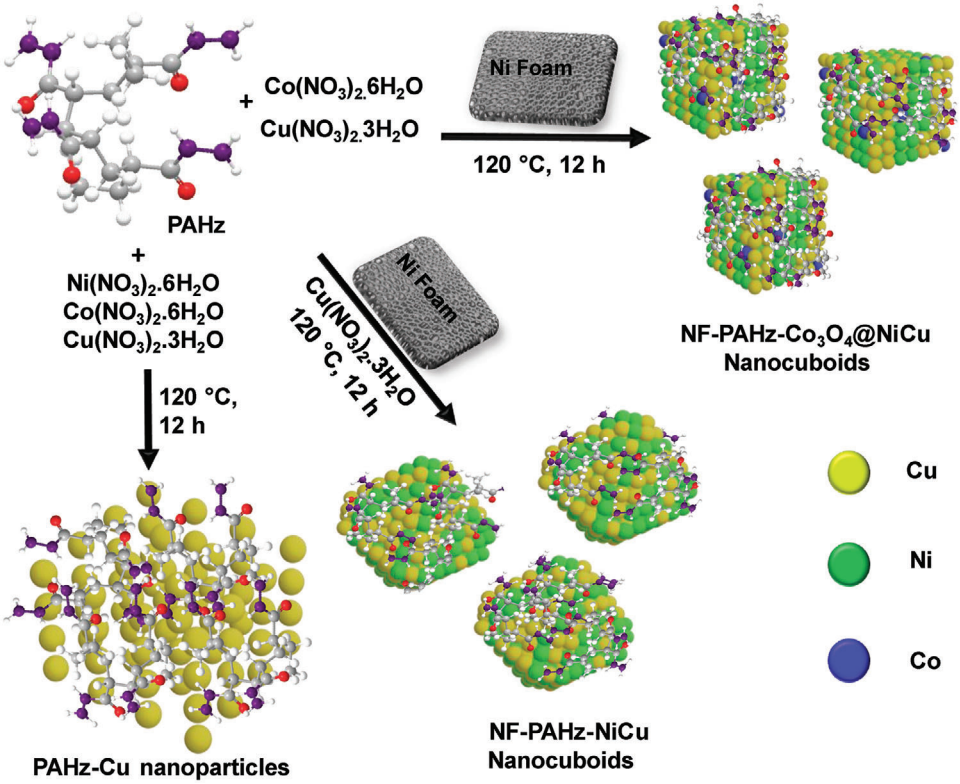

Scheme 1. The schematic procedure shows the synthesis of various nanostructures in the presence and absence of NF.

The XPS data of NF-PAHz-NiCu displayed Ni 2p and Cu 2p peaks at 852.6 and 932.7 eV corresponding to Ni(0) and Cu(0) respectively suggesting its possible structural similarity with NF-PAHz-Co_3O_4@NiCu (Figure S4, Supporting Information). The Cu 2p peak for the other control (PAHz-Cu) was observed at 932.9 eV suggesting the reduction of Cu^{2+} to Cu(0) and possible formation of PAHz-Cu nanocomposite (Figure S5, Supporting Information). Interestingly, the Ni 2p peaks were observed at 853.6 and 855.7 eV suggesting the presence of Ni^{2+} and Ni^{3+} and the formation of possible Ni oxide under the given conditions (Figure S5, Supporting Information). The ultraviolet photoelectron spectroscopy (UPS) data was analyzed to calculate the work function values of the catalysts (Figure 1G; Figure S6, Supporting Information). The work function values for the NF-PAHz-Co_3O_4@NiCu and NF-PAHz-NiCu were calculated to be 4.19 and 5.02 eV, respectively. Already active electrodes displaying proficiency toward OER and MOR activities have exhibited similar work function values in literature.[51,52] In the Cu K-Edge XANES data, the curve overlapped with that of the Cu foil in the near-edge region supporting the presence of Cu(0) in NF-PAHz-Co_3O_4@NiCu. A similar trend was also observed in the Cu K-edge data of NF-PAHz-NiCu supporting the similarity in oxidation state of Cu in both the above samples. The Cu K-edge FT-EXAFS data revealed that the Cu—Cu bond present at 12 coordination with radial distances of 2.57 Å in NF-PAHz-Co_3O_4@NiCu and 2.54 Å in NF-PAHz-NiCu, which is close to that of the Cu foil (2.54 Å) (Figure 1H,I).[53] The Ni K-edge position at half-maximum of the absorption for NF-PAHz-Co_3O_4@NiCu and NF-PAHz-NiCu exhibited a minor up-field shift compared to that of the Ni foil suggesting a possible change in an oxidation state of Ni(0) (Figure 1J). Considering the relatively small shift, the change in oxidation state may be considered as minor (< +1), which may be attributed to atmospheric oxidation of the Ni in the sample during the handling process.[54] Importantly, the Ni K-edge FT-EXAFS data revealed that the Ni—Ni bond is present at 12 coordination with the radial distance of 2.49 Å in NF-PAHz-Co_3O_4@NiCu and 2.48 Å in NF-PAHz-NiCu, which is similar to that of the Ni foil (2.48 Å) (Figure 1K).[55] Contrastingly, the Co K-edge data displayed a notable shift of 5.9 eV in the near-edge region supporting the presence of Co_3O_4 in NF-PAHz-Co_3O_4@NiCu (Figure 1L).[56] The Co K-edge FT-EXAFS data revealed that the Co–O present at 4 coordination with the radial distance of 1.98 Å in NF-PAHz-Co_3O_4@NiCu, which is 0.51 Å lower compared to that of the Co foil (2.49 Å) (Figure 1M).[57] Overall, the XRD, XPS, and XANES data supported the proposed structures of the NF-PAHz-Co_3O_4@NiCu and control samples. Possibly, in the presence of a mild reducing agent (PAHz), the Cu^{2+} with a positive reduction potential (E°): (Cu^{2+}/Cu ≈+0.34 V) preferably converted to the corresponding Cu(0), whereas Co^{2+} (E°: Co^{2+}/Co ≈−0.28 V) possessing propensity toward oxidation formed the corresponding oxide (Co_3O_4).[58] Cu^{2+} and Ni^{2+} in the presence of hydrazine are known to form Cu(0) and Ni(0), respectively under moderate temperature conditions,[59,60] whereas Co^{2+} requires a much stronger base such as NaOH along with hydrazine to form the corresponding Co(0).[61] In presence of NF, the Ni(0) from the NF surface participated in the NiCu alloy nancuboid formation, whereas in absence of NF, the PAHz-Cu nanocomposite was isolated and the amorphous oxides of Ni and

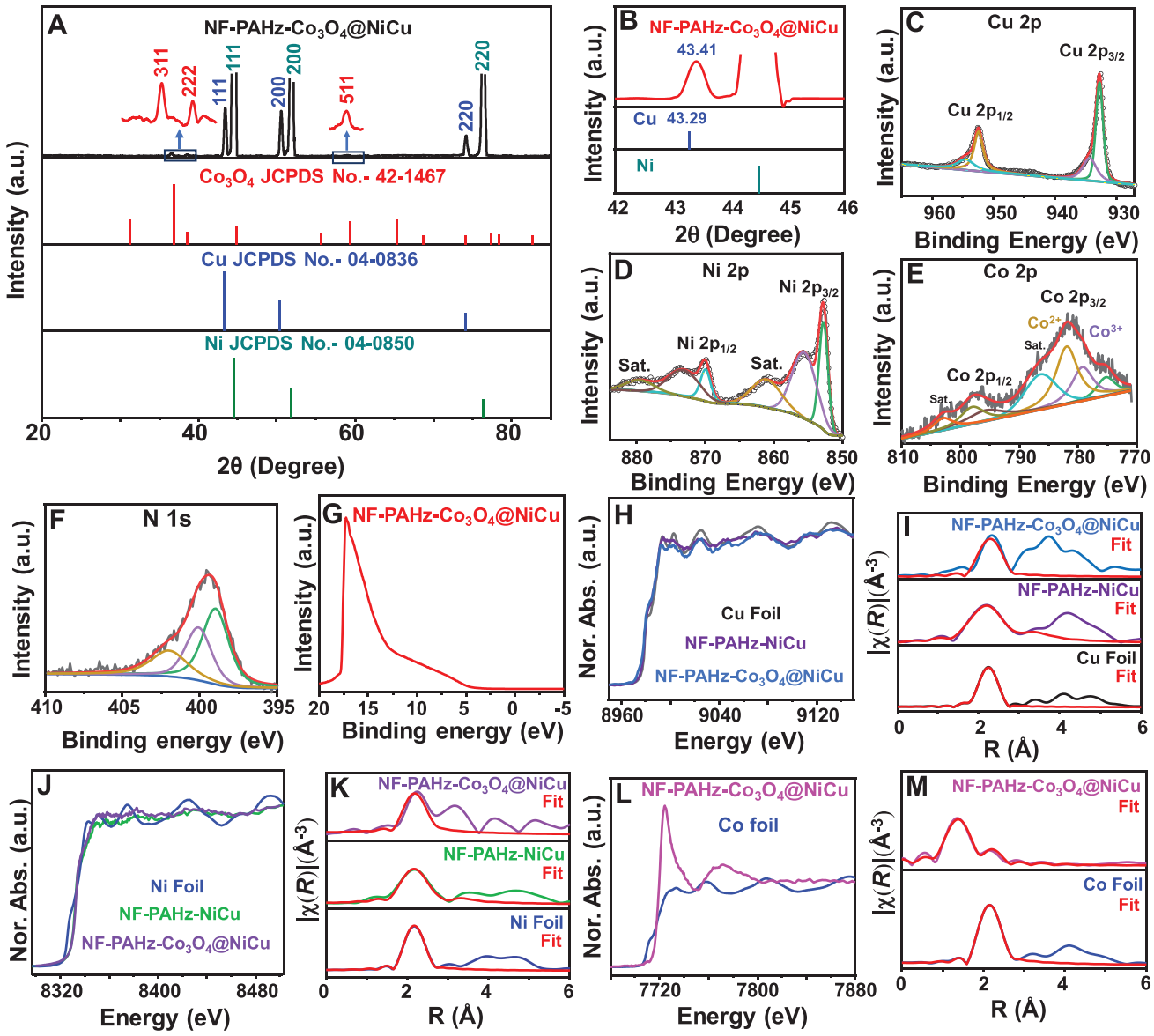

Figure 1. A) The XRD data of NF-PAHz-Co_3O_4@NiCu and the corresponding JCPDS traces, B) the XRD traces in "A" magnified in 42–46° 2θ region, the C) Cu 2p, D) Ni 2p, E) Co 2p and F) N 1s XPS spectra of NF-PAHz-Co_3O_4@NiCu, G) the UPS spectra of NF-PAHz-Co_3O_4@NiCu, the Cu K-edge H) X-ray absorption near edge structure (XANES) and I) Fourier transformed (FT)-Extended X-ray absorption fine structure (EXAFS) spectra, the Ni K-edge J) XANES and K) FT-EXAFS spectra, the Co K-edge L) XANES and M) FT-EXAFS spectra of NF-PAHz-Co_3O_4@NiCu.

Co possibly formed during the process remained in the aqueous phase.

The morphology of NF-PAHz-Co_3O_4@NiCu was then investigated using field emission scanning electron microscopy (FESEM) analysis. The NF-PAHz-Co_3O_4@NiCu displayed an irregular cuboid-type morphology (**Figure** 2A,B). The average width of these cuboids was observed ≈220 nm (Figure S7, Supporting Information). Another subsequent batch of NF-PAHz-Co_3O_4@NiCu was synthesized to understand the reproducibility of the shape and size of these nanocrystals. Satisfactorily, the uniform cuboid shapes were reproduced in the subsequent batch (Figure S8, Supporting Information). The FESEM-EDX data revealed that the amount of Cu (13.2%) is somewhat higher compared to that of the Ni (8.8%) in the NF-PAHz-Co_3O_4@NiCu (Figure S9, Supporting Information). The Co (0.3%) dopant was present in a relatively minor amount in the sample. The notable amount of C (53.7%), N (14.0%), and O (10.0%) supported the presence of PAHz chains in the sample, which possibly served as the capping agent and promoted the coalescence of NiCu alloy nanoparticles. The control sample synthesized in the absence of Co^{2+} (NF-PAHz-NiCu) also displayed cuboid morphology of various sizes with an average particle size (D_{avg}) of 212 nm (Figure 2C; Figure S10, Supporting Information). However, the control (PAHz-Cu) synthesized in the absence of NF and by taking different salts (Cu^{2+}, Ni^{2+}, and Co^{2+}) in the reaction medium failed to display any particular morphology suggesting that the

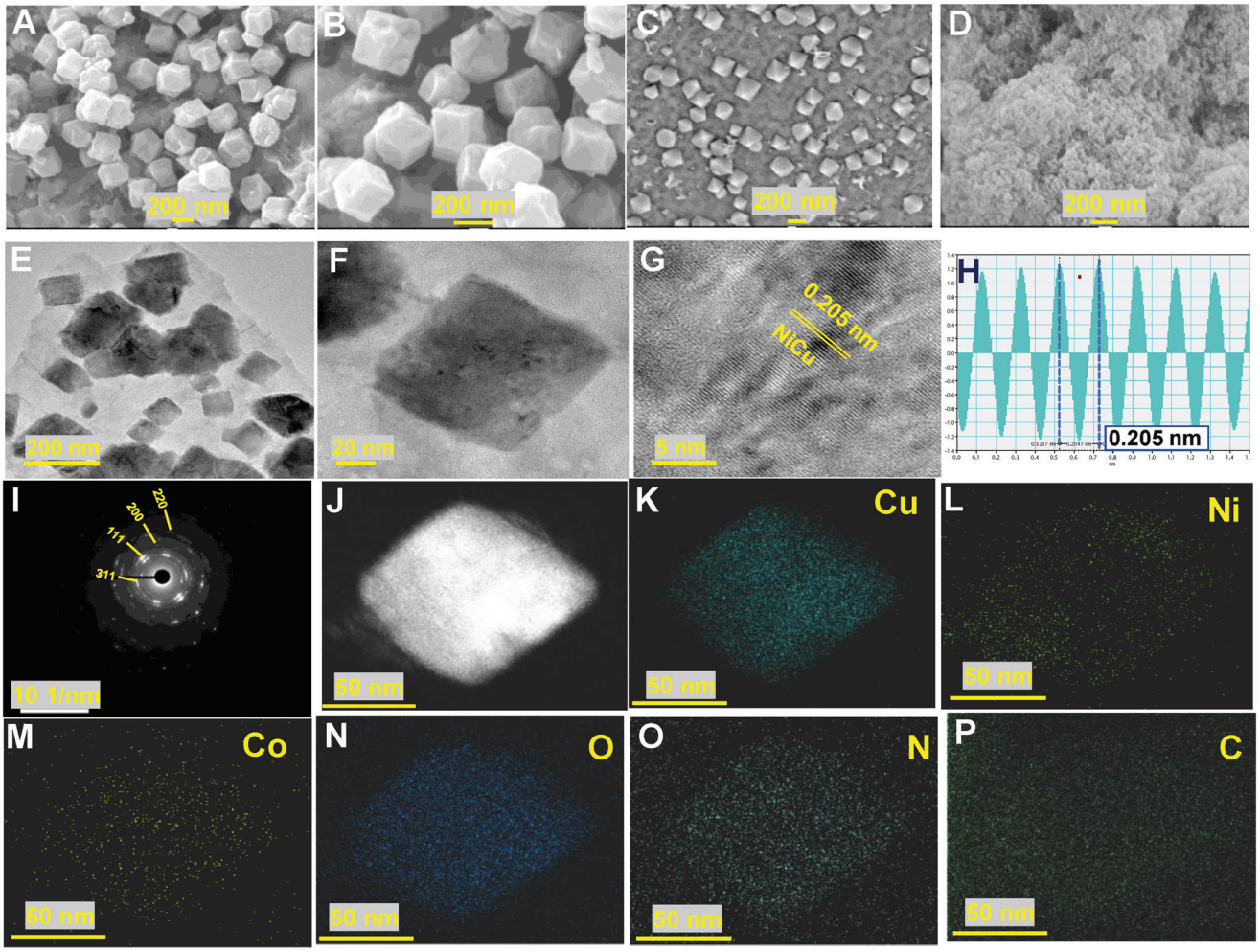

Figure 2. The A,B) FESEM images of NF-PAHz-Co_3O_4@NiCu at different magnifications, the FESEM images of C) NF-PAHz-NiCu & D) PAHz-Cu, the E,F) TEM images of NF-PAHz-Co_3O_4@NiCu at different magnifications, G) the d spacing value of PAHz-Co_3O_4@NiCu and H) the corresponding inverse fast fourier transform (IFFT) data, I) the TEM diffraction pattern of PAHz-Co_3O_4@NiCu, J–P) the HAADF-STEM elemental mapping of PAHz-Co_3O_4@NiCu.

NF surface possibly acted as the nucleating site and promoted the NiCu alloy cuboid formation under the experimental conditions (Figure 2D; Figure S11, Supporting Information). The high resolution transmission electron microscopy (HRTEM) data was subsequently recorded of NF-PAHz-Co_3O_4@NiCu. The images displayed cuboids of different sizes (D_{avg} ≈194 nm) supporting the SEM data (Figure 2E,F; Figure S12, Supporting Information). Interestingly, each of these cuboids displayed NiCu alloy nanocrystals of 3 to 6.5 nm sizes (D_{avg} ≈5 nm), which possibly underwent PAHz-aided segregation to realize the final shape (Figure S13, Supporting Information). The d spacing value of 0.205 nm corresponding to [111] plane was intermediate between Ni(0) (0.203 nm) and Cu(0) (0.209 nm) supporting the formation of NiCu alloy (Figure 2G,H).[62,63] The selected area electron diffraction (SAED) image displayed well resolved diffraction pattern supporting the crystallinity of these PAHz-Co_3O_4@NiCu nano-cuboids. The [111], [200], and [220] planes corresponding to NiCu alloy and [311] plane accountable to Co_3O_4 were visible in the image. (Figure 2I). The high-angle annular dark-field scanning transmission electron microscopy (HAADF-STEM) data revealed the presence of Cu in major amount in the NF-PAHz-Co_3O_4@NiCu cuboids followed by Ni and Co (Figure 2J–P). Considerable amounts of N, C, and O further supported the presence of PAHz chains in these cuboid matrixes.

Overall, a number of characterization data suggested that both Ni surface and PAHz chains promoted the growth of NiCu alloy-based cuboids on the surface. Alloy nanoparticles are known to form in aqueous solution via co-reduction of multiple metal salts.[64] Furthermore, the Ni(0) in the presence of Cu^{2+} is known to undergo a redox reaction to form Ni^{2+} and Cu(0) under hydrothermal conditions.[65] PAHz is known to self-assemble in an aqueous solution to form spherical aggregates[66] and readily reduce various metal salts to the corresponding PAHz-capped metal nanoparticles in aqueous solution.[29,30,33] Considering the above factors, a plausible mechanism for the formation of possible NiCu alloy in the PAHz matrix is proposed under the reaction conditions (Figure S14, Supporting Information). However, in the absence of NF, PAHz-Cu composites with random

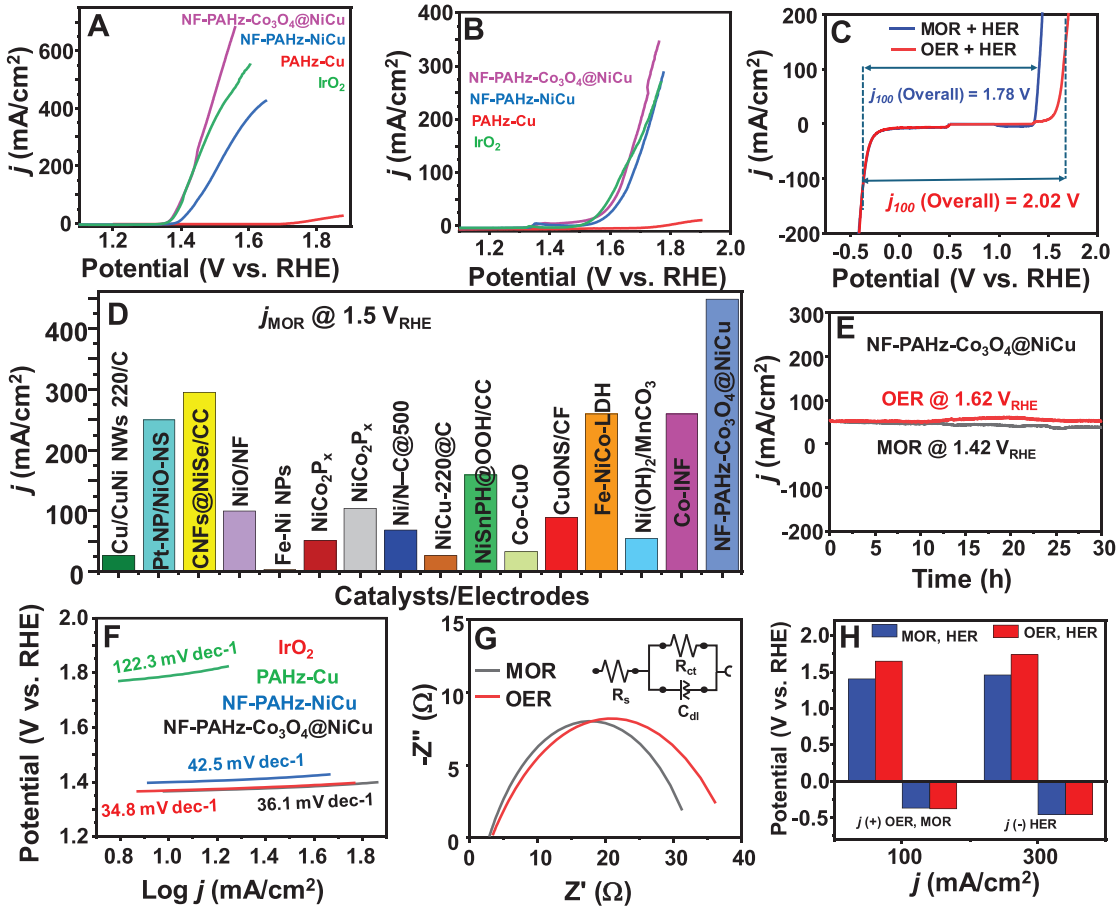

Figure 3. A) The MOR and B) OER traces of NF-PAHz-Co_3O_4@NiCu, control and reference electrodes, C) the overall water splitting curves of NF-PAHz-Co_3O_4@NiCu MOR and OER based processes, D) the comparison of MOR j value at 1.5 V_{RHE} of NF-PAHz-Co_3O_4@NiCu with that of the recently reported systems, E) the chronoamperometry traces of NF-PAHz-Co_3O_4@NiCu showing the MOR and OER stability, F) the Tafel slope values of NF-PAHz-Co_3O_4@NiCu and controls recorded for MOR process, G) the Nyquist fits of NF-PAHz-Co_3O_4@NiCu obtained during MOR and OER operation, H) the comparison of j and potential values between MOR and OER operations for NF-PAHz-Co_3O_4@NiCu.

morphology were witnessed. To further understand the effect of PAHz concentration on the shape and sizes of resulting nanostructures, the NF-PAHz-Co_3O_4@NiCu was synthesized in the presence of 4 and 6 wt.% PAHz solutions. In both cases, cuboid structures were observed in the FESEM images similar to that of the 2 wt.% solution (Figure 2A; Figure S15, Supporting Information). However, the sizes of these cuboids were observed to be different in each of the cases. The NF-PAHz-Co_3O_4@NiCu were also synthesized in the presence of different [Cu^{2+}] amounts. On increasing the [Cu^{2+}] from 16.5 to 24.8 mM in solution, the resulting sample exhibited a cuboid shape and the average size somewhat decreased to 208 nm (Figure S16, Supporting Information). However, at a low [Cu^{2+}] (8.2 mM) amount in solution, no formation of cuboid shape was witnessed and the resulting sample appeared as a cluster of nanoparticles (average size ≈162.7 nm) (Figure S17, Supporting Information).

These nanocuboids with sharp edges and the exposed prominent [111] plane were anticipated to exhibit swift electrocatalytic activity.[67,68] The electrocatalytic activity of the electrodes was subsequently assessed by studying MOR and OER reactions. The MOR activities were carried out in 1.0 M KOH and 1.0 M MeOH aqueous solution using NF-PAHz-Co_3O_4@NiCu and graphite as working and counter electrodes respectively. The electrode exhibited superior MOR activity and j value of 100 mA cm^{-2} was realized at a potential value of 1.41 V_{RHE} (**Figure 3A**). However, a similar j_{MOR} value for NF-PAHz-NiCu was realized at a higher potential of 1.46 V_{RHE} and the PAHz-Cu failed to produce j value of 100 mA cm^{-2} till 2.0 V_{RHE} suggesting the Co_3O_4 doping and the shape of the nanocatalyst possibly promoted the MOR activity. The electrochemical active surface area (ECSA) data also revealed that the value for NF-PAHz-Co_3O_4@NiCu (28.5 cm^2) is superior compared to that of the NF-PAHz-NiCu (16.8 cm^2) supporting the higher activity of the former (Figures S18, S19 and Table S1, Supporting Information). Similarly, the NF-PAHz-Co_3O_4@NiCu electrode displayed adequate OER activity in 1.0 M KOH solution and j_{OER} value of 100 mA cm^{-2} was observed at 1.65 V_{RHE}. Importantly, the potential value was inferior by 0.24 V compared to that of the j_{MOR} at 100 mA cm^{-2} suggesting the superior energy efficiency of the MOR process (Figure 3B). The potential difference value (0.28 V) between MOR and OER was more pronounced at high j value of 300 mA cm^{-2}. The $j_{MOR+HER}$ value of 100 mA cm^{-2} was realized at 1.78 V_{RHE} overall

potential for MOR process, whereas for OER based process, the value was realized at 2.02 V suggesting the former offering an effective energy-efficient option for green H_2 production (Figure 3C). The MOR (j_{10} at 1.37 V_{RHE}) and OER (j_{10} at 1.52 V_{RHE}) activities of NF-PAHz-Co_3O_4@NiCu were comparable to that of the benchmark IrO_2 ($j_{10,\ MOR}$ at 1.37 V_{RHE} and $j_{10,\ OER}$ at 1.54 V_{RHE}) supporting the efficacy of the developed electrodes for related applications (Figure S20, Supporting Information). The j_{MOR} value realized at 1.5 V_{RHE} for several catalyst compositions reported in literature was compared to that of the NF-PAHz-Co_3O_4@NiCu. The j_{MOR} value (448 mA cm^{-2}) of the current electrode was superior compared to that of the several recently reported systems (Figure 3D; Table S2, Supporting Information). The stability of NF-PAHz-Co_3O_4@NiCu was assessed for MOR activity and the chronoamperometry data at a potential value of 1.42 V_{RHE} revealed a minor loss (≈20%) in activity over 30 h period supporting adequate durability (Figure 3E). The above minor loss in j value may be assigned to the gradual decrease in MeOH concentration in the electrolyte over the period.[69] Importantly, the OER durability data at potential = 1.62 V_{RHE} revealed no change in j value over 30 h period further supporting the sustainability of the electrode for both processes.

The low MOR Tafel slope value (36.1 mV dec^{-1}) of NF-PAHz-Co_3O_4@NiCu compared to that of the NF-PAHz-NiCu (42.5 mV dec^{-1}) and PAHz-Cu (122.3 mV dec^{-1}) supported the higher activity of the former (Figure 3F). Similarly, the Nyquist plots of the NF-PAHz-Co_3O_4@NiCu revealed the R_s values of 2.8 and 3.3 Ω for MOR and OER activities respectively, which was lower compared to that of NF-PAHz-NiCu (R_s of MOR: 2.9 Ω) supporting the possible role of Co_3O_4 doping toward higher conductivity (Figure 3G). The study revealed that the overall potential required to carry the operation at j ≈300 mA cm^{-2} using MOR as the anode half-reaction is 1.92 V, which is superior by 0.28 V compared to that of the conventional OER-based process (Figure 3H). These studies amply demonstrated the ability of the NF-PAHz-Co_3O_4@NiCu to produce MOR-promoted green H_2 in an energy-efficient manner. Furthermore, the shape of nanocuboids, the Co_3O_4 doping, and the active site of Cu synergistically contributed toward the above superior catalytic activity of NF-PAHz-Co_3O_4@NiCu. However, no significant change in the MOR activities of NF-PAHz-Co_3O_4@NiCu electrodes synthesized in the presence of higher PAHz amounts (4 and 6 wt.%) ($j_{100,MOR}$ at ≈1.43 V_{RHE}) was witnessed compared to that of the 2 wt.% electrode ($j_{100,MOR}$ at 1.41 V_{RHE}) (Figure S21, Table S3, Supporting Information). The OER activities also followed a similar trend for the electrodes synthesized in the presence of different PAHz amounts in solution. Interestingly, the HER activity of the electrode synthesized using 6 wt.% PAHz solution was marginally superior compared to the other compositions. An overall comparison of MOR, OER and HER data of all the compositions revealed that the electrode synthesized using 2 wt.% PAHz (NF-PAHz-Co_3O_4@NiCu) may be suitable for further purposes. Subsequently, the catalytic activities of NF-PAHz-Co_3O_4@NiCu synthesized in the presence of different Cu^{2+} amounts were assessed. The MOR and OER activities of NF-PAHz-Co_3O_4@NiCu were somewhat superior compared to that of the other compositions synthesized at higher (24.8 mM) and lower (8.3 mM) Cu^{2+} amounts (Figure S22, Table S4, Supporting Information). Importantly, the HER activity of the electrode synthesized using 24.8 mM Cu^{2+} was superior compared to that of the other compositions. Overall, the NF-PAHz-Co_3O_4@NiCu synthesized using Cu^{2+} ≈16.5 mM was advantageous among the different compositions based on the overall catalytic activity and cost-effectiveness of the synthesis.

The processes were then carried out under two-electrode mode to mimic the electrolyzer setup (**Figure 4A**). The j_{MOR} value of 10 mA cm^{-2} was achievable at 1.62 V, whereas the same j value for OER based process was realized at 1.76 V (Figure 4B). The chronoamperometry data recorded at 1.62 V revealed no noticeable change in $j_{MOR+HER}$ value (10 mA cm^{-2}) for 100 h suggesting the sustainability of the electrode (Figure 4C). The stability of OER based process was also monitored under 2-electrode mode using NF-PAHz-Co_3O_4@NiCu as both working and counter electrodes. The data revealed no appreciable change in $j_{OER+HER}$ value for 100 h supporting the above (Figure 4D). Lastly, the faradaic efficiency value for produced H_2 under two electrode modes for MOR was calculated to be 93.2% (Figure 4E). The faradaic efficiencies for the production of O_2 and H_2 in OER based procedure were also effective (Figure 4F).

To understand the product/s formed during the MOR, the ^1H NMR analysis of the electrolyte was carried out in D_2O. A new singlet at 8.3 ppm for H–COO^- supported the formation of formate in the solution (Figure 4G). The comparison between the integrations of resonances at 3.1 ppm (H_3C–OH) and 8.3 ppm revealed that after 96 h of MOR operation, ≈71.6% conversion was realized (Figure S23, Supporting Information).[70] Importantly, no other peaks were visible in the spectra supporting the selectivity of product formation. ^{13}C NMR Peaks at 171 and 168 ppm corresponding to $HCOO^-$ and HCOOH, respectively supported the formation of formate during the electrochemical process. The FT-IR band at 1639 cm^{-1} for C=O also supported the formate formation. (Figure 4H). The ^{13}C NMR spectra of the electrolyte after different time intervals were recorded to understand the possibility of CO/CO_2 formation during the process. Interestingly, the absence of resonance ≈162 ppm probably excluded the possibility of the formation of CO_2 during the process (Figure S24, Supporting Information).[71]

To gain further insight into the superior activity, density functional theory (DFT) calculations were undertaken to calculate the Gibb's free energy changes (ΔG) of NF-PAHz-Co_3O_4@NiCu and control electrodes. At OER's equilibrium potential, the ΔG values for the different elementary steps were computed using the method described in literature.[72,73] Ni (111) and Cu (111) double layers were placed upon each other to study the OER activity on Ni and Cu sites in the NiCu alloy (Figure S25, Supporting Information). Subsequently, the respective sites were doped with Co and its oxide, and the change in ΔG profile was assessed (**Figure 5A,B**, Figure S26, Supporting Information).[74] The ΔG profiles for different OER stages under the catalytic roles of NiCu, Co@NiCu, and Co-O@NiCu are shown in (Figure 5C,D). The M–O^* to M–OOH^* step was observed to be the rate-determining step for all the different systems studied. In the case of OER activity at Cu site, the rate-determining step energy barrier of NiCu alloy was 2.80 eV which reduced to 2.63 and 2.24 eV with Co and Co oxide doping respectively (Figure 5C). Similarly, in the case of OER activity at the Ni site, the ΔG value for the rate-determining step was 3.30 eV, which decreased to 3.09 and 2.91 eV with Co and the Co oxide doping respectively (Figure 5D). Interestingly, the

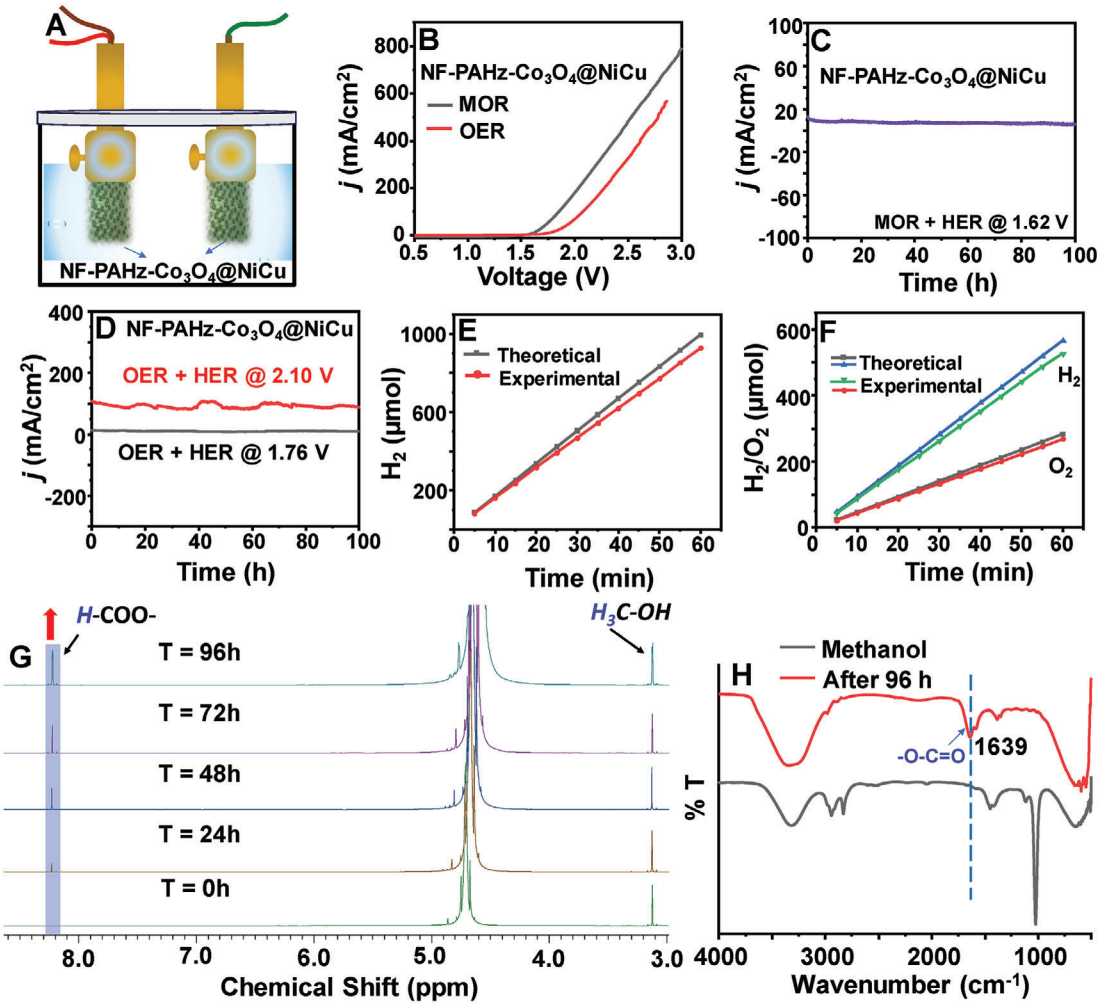

Figure 4. A) The schematics showing the two-electrode setup for MOR coupled H_2 production using NF-PAHz-Co_3O_4@NiCu as working and counter electrodes, B) the linear sweep voltammetry (LSV) for OER and MOR-based procedures in two-electrode set up, the chronoamperometry trace of the C) MOR based process recorded at 1.62 V and D) OER based process recorded at 1.76 and 2.10 V in two-electrode set up, the theoretical and experimental H_2 production data in E) MOR and F) OER based procedure, G) the ^{1}H nuclear magnetic resonance (NMR) and H) FT-infra red (IR) spectra of the electrolyte solution recorded after regular time intervals during MOR operation.

study revealed that the activity at the Cu site in the NiCu alloy was associated with a lower ΔG value at the rate-determining step compared to that of the Ni site. Additionally, the Co oxide doping further decreased the ΔG value supporting the experimental observation and superior OER activity of NF-PAHz-Co_3O_4@NiCu. The lowest ΔG value (2.24 eV) for the Co oxide doped at the Cu site revealed that possibly in the NiCu alloy the Cu served as the active site to initiate the OER and MOR process.

To verify the results, the partial density of states (PDOS) of NiCu and Co & Co oxide doped NiCu were calculated. The presence of continuous density of state (DOS) around the Fermi level supported the intrinsic metallic characteristics of the pure and doped NiCu. For the Co and Co oxide doped NiCu, the DOS broadened near the Fermi level compared to that of the pure NiCu. For both the active sites (Ni and Cu sites) of the catalyst, the broadening of the DOS at the Fermi level is maximum for the Co oxide doped NiCu catalyst (Figure 5E,F). The introduction of Co and O atoms to NiCu helped to enhance the DOS near the fermi level, which increased the charge carrier concentration. Hence, Co oxide doped NiCu in this instance enabled significantly faster electron transfer and demonstrated more conducting pathways, entrusting them with faster kinetics and improved OER activity.[75] The MOR activities were subsequently calculated on the Cu site for Co-O@NiCu under an alkaline environment (Figure 5G). The conversion of $^*CH_3O$ to $^*CH_2O$ was determined to be the rate-determining step and the process was endothermic by 0.31 eV with an energy barrier of 1.02 eV (Figure 5H).[76]

3. Conclusion

The metallic Ni surface serves as the shape-directing avenue during the PAHz mediated in situ reduction of Cu and Ni salts to the corresponding NiCu alloy nanocrystals under hydrothermal conditions. The methodology allows growth of NiCu alloy and in situ doping of metal oxides on the alloy surface in a one-pot procedure. The resulting electrodes exhibit swift MOR

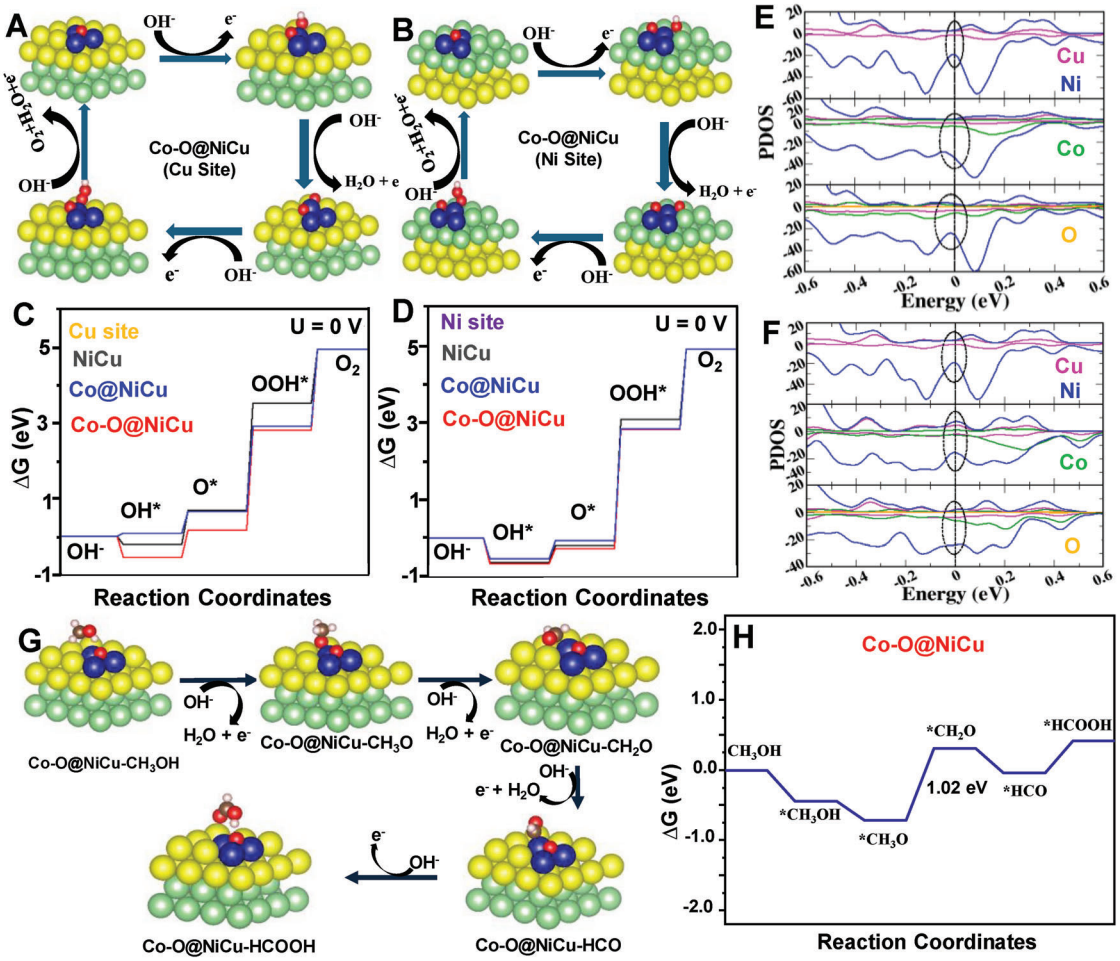

Figure 5. Schematic diagrams of the OER activity of the Co-O doped on the A) Cu and B) Ni site of Co-O@NiCu, Gibb's free energy diagrams for the OER activities of NiCu, Co@NiCu, and Co-O@NiCu calculated for C) Cu site and D) Ni site respectively, PDOS of NiCu, Co@NiCu, and Co-O@NiCu obtained for E) Cu site and F) Ni site, G) Schematics showing the various steps of MOR activity on the Co-O@NiCu operated at Cu site, H) the Gibb's free energy diagrams for the MOR activities on Co-O@NiCu calculated on Cu site. The * represents the active site of the catalyst and *CH_3OH, *CH_3O, *CH_2O, *HCO, *HCOOH represent the respective species adsorbed on the active site.

and OER activities under alkaline conditions and are suitable for bi-functional MOR and OER coupled energy efficient green H_2 production. Possibly, the active Cu site in NiCu heterostructure, Co_3O_4 doping, and the sharp edges of the nanocuboids synergistically contribute toward the effective electrocatalytic activity. The NF-PAHz-Co_3O_4@NiCu produces formate/formic acid from methanol in relatively high yields. The theoretical DFT analysis predicted that the Cu site in the NiCu nanocrystal acts as the active center for the OER activity. The synthetic strategy is general and may be utilized to grow other alloy nanocrystals for use as catalysts in electrochemical operations.

4. Experimental Section

Material Required: Nickel (II) nitrate hexahydrate (98%, Sigma–Aldrich), copper (II) nitrate trihydrate (97%, Fisher Scientific), cobalt (II) nitrate hexahydrate (98%, Sigma–Aldrich), NF (99%, thickness 1.6 mm, Goodfellow), potassium hydroxide (98%, Qualigens,), hydrazine hydrate (99%, Rankem), tetra-n-butylammonium bromide (98%, Merck), methanol (99%, Finar), tetrahydrofuran (99%, Finar Ltd.), ethanol (99%, Changshu HFCL), hydrochloric acid (99%, SDFCL) were used as received. DI water was obtained from the Millipore water purification system.

Material Characterization: The XRD diffraction data was recorded using a Pananalytical Empyrean X-ray diffractometer in the 2Θ range of 10–90°. A monochromatic Al K-Alpha analyzer (XPS, ThermoFisher) corrected with C1s 284.8 eV was used to analyze the surface electronic properties. The surface morphology of the material was analyzed using FESEM (JSM-7900F, Jeol Ltd. and the elemental distribution analysis were done using the (JSM-7900F, Jeol Ltd.) energy dispersive X-ray spectroscopic (EDX) technique. The HRTEM (JEM-F200 JEOL) was used to acquire the high-resolution images along with the STEM-HAADF and SAED images. The ^1H and ^{13}C NMR spectroscopic data were obtained utilizing an NMR JEOL 400 YH machine operated at a temperature of 25 °C in the solvent D_2O. The FT-IR spectroscopic data were recorded in a PerkinElmer Spectrum Two instrument in ATR mode. Materials were characterized using X-ray absorption spectroscopy (XAS) at the INDUS beamline synchrotron facility (2.5 GeV, 100 mA), BL-09, INDUS-2.

Synthesis of NF-PAHz-Co_3O_4@NiCu: The NF-PAHz-Co_3O_4@NiCu electrode fabrication process consisted of the following. Initially, the NF with the dimension of 2.5 × 3.0 cm^2 was cleaned with hydrochloric acid (24 mL, 2 M), ethanol (20 mL), and DI water (20 mL) to eliminate

any impurities present on the surface. Subsequently, $Cu(NO_3)_2.3H_2O$ solution (50 mL, 16.55 mM) was taken in a beaker at room temperature and kept under constant stirring at 700 rpm. To this, 25 mL of a 2 wt.% PAHz solution was supplemented and the solution was left undisturbed for 60 min. A solution of $Co(NO_3)_2.6H_2O$ (50 mL, 13.74 mM) was introduced into the above solution and the resulting solution was kept under stirring for 30 min. To this additional 25 mL of the 2 wt.% PAHz solution was added and the whole mixture was kept under stirring for 60 min. An autoclave was filled with this resulting homogeneous mixture and the above piece of cleaned NF was immersed into it. The autoclave was now left in a hot air oven at 120 °C for 12 h. Subsequently, the temperature of the system was cooled to room temperature. The NF was removed from the aqueous solution and washed with DI water. The sample was then dried in a vacuum oven for 12 h at 50 °C.

Synthesis of NF-PAHz-NiCu: The surface of NF was activated using the procedure stated above using hydrochloric acid (24 mL, 2 M), ethanol (20 mL), and DI water (20 mL). A $Cu(NO_3)_2.3H_2O$ aqueous solution (50 mL, 16.55 mM) was placed in a beaker and stirred at a continuous stirring speed of 700 rpm at room temperature. Subsequently, 25 mL of 2 wt.% PAHz solution was added gradually to the above solution over a period of an hour. This homogeneous mixture was transferred into an autoclave possessing NF. Subsequently, the autoclave was heated in a hot air oven at 120 °C for 12 h. The NF was then removed from the solution, washed with the DI water, and dried at 50 °C.

Synthesis of PAHz-Cu: PAHz aqueous solution (25 mL of 2 wt.%) was added dropwise over a period of an hour under a constant stirring rate of 700 rpm to $Cu(NO_3)_2.3H_2O$ solution (50 mL, 16.55 mM). Subsequently, $Co(NO_3)_2.6H_2O$ (50 mL, 13.74 mM) solution was added directly to the above solution over a 30 min period. Subsequently, 25 mL of 2 wt.% PAHz was added in a dropwise manner over a period of one hour to the above solution. Then $Ni(NO_3)_2.6H_2O$ solution (50 mL, 13.75 mM) was added to the above resulting solution over one-hour period. The resultant solution was put into an autoclave and kept in a hot air oven for 12 h at 120 °C. The precipitate obtained was filtered. The filtrate was repeatedly cleaned with deionized (DI) water and kept in a vacuum oven set at 50 °C for 12 h.

Electrochemical Measurements: All the electrochemical analysis was carried out using an electrochemical workstation (M204 PGSTAT, Autolab). The electrochemical measurements were conducted using a 25 mL mini gas-tight cell. A three-electrode system was employed, with the NF-PAHz- Co_3O_4@NiCu electrode as working, graphite rod as a counter electrode, and Hg/HgO (1.0 M NaOH) as a reference electrode. The electrolyte used for OER and HER was 1.0 M KOH, while a 1.0 M MeOH + 1.0 M KOH solution was used for MOR and HER. NMR spectroscopic data were collected at regular intervals of 24 h throughout the chronoamperometry test at 1.86 V to observe the change during methanol-to-formate formation. Nernst equation was utilized to transform the potential on the RHE scale. The obtained current was converted into *j* (current density) and standardized with the working electrode's geometrical area.

$$E_{RHE} = E^0_{Hg/HgO} + E_{Hg/HgO} + 0.0591 \times pH \quad (1)$$

Fabrication of PAHz-Cu Electrode: First, 0.75 mL of deionized water was combined with 0.25 mL of methanol to make a solution. To this solution, 20 mg of PAHz-Cu was added along with 0.2 mL of 5 wt.% Nafion solution. This mixture was then subjected to ultrasonic treatment for 1 h to disperse the components and form a well-mixed ink suspension. Subsequently, a glassy carbon electrode with a diameter of 5 mm was coated with 6 µL of the aforementioned ink suspension via drop casting. The drop-cast film was allowed to dry in at hot air oven at 50 °C for overnight.

Fabrication of IrO_2 and Pt/C Electrode: Commercial Pt/C and IrO_2 of 6.0 mg each was dissolved in 1.35 mL of a mixture of isopropanol (0.80 mL), water (0.40 mL), and 5 wt.% Nafion (0.15 mL) separately and sonicated for 50 min to make homogeneous inks. Then, one of the catalyst ink (100 µL) was drop coated onto the surface of the NF electrodes and dried in vacuum oven for overnight at 50 °C.

Supporting Information

Supporting Information is available from the Wiley Online Library or from the author.

Acknowledgements

The financial assistance from SERB (CRG/2022/002067) is gratefully acknowledged. The authors acknowledge the CIF, RGIPT for instrumental analysis and IOP Bhubaneswar for HPC facility. The authors are also grateful to Dr. Biplab Ghosh of Beamline Development and Application Section, BARC, Mumbai for their valuable support toward EXAFS measurements at Scanning EXAFS beamline (BL-09) Indus-2, RRCAT, Indore, India.

Conflict of Interest

The authors declare no conflict of interest.

Data Availability Statement

The data that support the findings of this study are available on request from the corresponding author. The data are not publicly available due to privacy or ethical restrictions.

Keywords

green H_2, methanol oxidation reaction, nanoalloy, nanocatalyst, oxygen evolution reaction

Received: May 28, 2024
Revised: August 13, 2024
Published online:

[1] M. van der Spek, C. Banet, C. Bauer, P. Gabrielli, W. Goldthorpe, M. Mazzotti, S. T. Munkejord, N. A. Røkke, N. Shah, N. Sunny, D. Sutter, J. M. Trusler, M. Gazzani, *Energy Environ. Sci.* **2022**, *15*, 1034.
[2] Y. Luo, Z. Zhang, M. Chhowalla, B. Liu, *Adv. Mater.* **2022**, *34*, 2108133.
[3] Z.-Y. Yu, Y. Duan, X.-Y. Feng, X. Yu, M.-R. Gao, S.-H. Yu, *Adv. Mater.* **2021**, *33*, 2007100.
[4] A. Tewary, S. Mandal, Z. Alam, A. S. K. Sinha, U. Ojha, A. C. S. Sustain, *Chem. Eng.* **2023**, *11*, 6556.
[5] L. Lin, W. Zhou, R. Gao, S. Yao, X. Zhang, W. Xu, S. Zheng, Z. Jiang, Q. Yu, Y.-W. Li, C. Shi, X.-D. Wen, D. Ma, *Nature* **2017**, *544*, 80.
[6] X. Han, H. Sheng, C. Yu, T. W. Walker, G. W. Huber, J. Qiu, S. Jin, *ACS Catal.* **2020**, *10*, 6741.
[7] J. Li, L. Li, J. Wang, A. Cabot, Y. Zhu, *ACS Energy Lett.* **2024**, *9*, 853.
[8] E. A. Paredes-Salazar, A. Calderón-Cárdenas, H. Varela, *ACS Catal.* **2023**, *13*, 9366.
[9] J. Wang, B. Zhang, W. Guo, L. Wang, J. Chen, H. Pan, W. Sun, *Adv. Mater.* **2023**, *35*, 2211099.
[10] M. Li, X. Deng, K. Xiang, Y. Liang, B. Zhao, J. Hao, J. Luo, X. Fu, *ChemSusChem* **2020**, *13*, 914.
[11] Y. Liu, E. Zhu, J. Huang, A. Zhang, A. H. Shah, Q. Jia, M. Xu, E. Liu, Q. Sun, X. Duan, Y. Huang, *Nano Lett.* **2023**, *23*, 2758.
[12] P. Deshpande, B. L. V. Prasad, *ACS Appl. Mater. Interfaces* **2023**, *15*, 26554.
[13] K. Liu, C. Zhang, Y. Sun, G. Zhang, X. Shen, F. Zou, H. Zhang, Z. Wu, E. C. Wegener, C. J. Taubert, J. T. Miller, Z. Peng, Y. Zhu, *ACS Nano* **2017**, *12*, 158.

[14] S. Ma, P. Yang, J. Chen, Z. Wu, X. Li, H. Zhang, *J. Colloid Interface Sci.* **2023**, *642*, 604.
[15] J. Dong, X. Zhang, J. Huang, J. Hu, Z. Chen, Y. Lai, *J. Chem. Eng.* **2021**, *412*, 128556.
[16] Y. Fu, H. Yu, C. Jiang, T. Zhang, R. Zhan, X. Li, J. Li, J. Tian, R. Yang, *Adv. Funct. Mater.* **2018**, *28*, 1705094.
[17] Z. Zhou, Y. H. Ng, S. Xu, S. Yang, Q. Gao, X. Cai, J. Liao, Y. Fang, S. Zhang, *ACS Appl. Mater. Interfaces* **2021**, *13*, 37299.
[18] D. Wu, W. Zhang, D. Cheng, *ACS Appl. Mater. Interfaces* **2017**, *9*, 19843.
[19] Y. An, H. Ijaz, M. Huang, J. Qu, S. Hu, *Dalton Trans.* **2020**, *49*, 1646.
[20] Q. Shao, Y. Li, X. Cui, T. Li, H.-G. Wang, Y. Li, Q. Duan, Z. Si, A. C. S. Sustain, *Chem. Eng.* **2020**, *8*, 6422.
[21] P. G. M. Mileo, S. Yuan, S. Ayala, P. Duan, R. Semino, S. M. Cohen, K. Schmidt-Rohr, G. Maurin, *J. Am. Chem. Soc.* **2020**, *142*, 10863.
[22] L. M. Bronstein, G. Goerigk, M. Kostylev, M. Pink, I. A. Khotina, P. M. Valetsky, V. G. Matveeva, E. M. Sulman, M. G. Sulman, A. V. Bykov, N. V. Lakina, R. J. Spontak, *J. Phys. Chem. B* **2004**, *108*, 18234.
[23] Y. Gu, M. Huang, W. Zhang, M. A. Pearson, J. A. Johnson, *Angew. Chem., Int. Ed.* **2019**, *58*, 16676.
[24] A. Venugopal, L. H. T. Egberts, J. Meeprasert, E. A. Pidko, B. Dam, T. Burdyny, V. Sinha, W. A. Smith, *ACS Energy Lett.* **2022**, *7*, 1586.
[25] A. M. Alsharabasy, A. Pandit, P. Farràs, *Adv. Mater.* **2021**, *33*, 2003883.
[26] S. M. S. Rana, M. A. Zahed, M. T. Rahman, M. Salauddin, S. H. Lee, C. Park, P. Maharjan, T. Bhatta, K. Shrestha, J. Y. Park, *Adv. Funct. Mater.* **2021**, *31*, 2105110.
[27] A. A. A. Abdelazeez, M. Rabia, F. Hasan, V. Mahanta, E. R. Adly, *Adv. Energy Sustainability Res.* **2024**, 2400077.
[28] D. V. Morales, C. N. Astudillo, V. Anastasoaie, B. Dautreppe, B. F. Urbano, B. L. Rivas, C. Gondran, D. Aldakov, B. Chovelon, D. André, J.-L. Putaux, C. Lancelon-Pin, S. Sirach, E.-M. Ungureanu, C. Costentin, M.-N. Collomb, J. Fortage, *Sustain. Energy Fuel.* **2021**, *5*, 4710.
[29] R. Rizo, B. R. Cuenya, *ACS Energy Lett.* **2019**, *4*, 1484.
[30] A. H. Al-Naggar, N. M. Shinde, J.-S. Kim, R. S. Mane, *Coord. Chem. Rev.* **2023**, *474*, 214864.
[31] R. R. Ujjwal, M. P. Purohit, S. Patnaik, U. Ojha, *ACS Appl. Mater. Interfaces* **2015**, *7*, 11497.
[32] R. R. Ujjwal, C. Sona, S. Debnath, P. N. Yadav, U. Ojha, *ACS Omega* **2017**, *2*, 4278.
[33] S. Yuan, F. Ge, Y. Chen, Z. Cai, *RSC. Adv.* **2017**, *7*, 6358.
[34] S. Mandal, A. Seth, V. Yadav, S. Kumari, M. Kumar, U. Ojha, *ACS. Appl. Polym. Mater.* **2019**, *2*, 618.
[35] S. S. Shin, Y. Jung, S. Jeon, S.-J. Park, S.-J. Yoon, K.-W. Jung, J.-W. Choi, J.-H. Lee, *Nat. Commun.* **2024**, *15*, 3889.
[36] J. H. Jo, S. S. Shin, S. Jeon, S.-J. Park, H. Park, Y.-I. Park, J.-H. Lee, *J. Chem. Eng.* **2022**, *449*, 137883.
[37] L. Zhang, X. Zha, G. Zhang, J. Gu, W. Zhang, Y. Huang, J. Zhang, T. Chen, *J. Mater. Chem. A* **2018**, *6*, 10217.
[38] P.-Y. Tang, Y.-Q. Zhao, Y.-M. Wang, C.-L. Xu, *Nanoscale* **2013**, *5*, 8156.
[39] A. Gopalakrishnan, L. Durai, J. Ma, C. Y. Kong, S. Badhulika, *Energy Fuels* **2021**, *35*, 10169.
[40] H. Jiang, L. Ai, M. Chen, J. Jiang, *ACS. Sustain. Chem. Eng.* **2020**, *8*, 10833.
[41] K. S. Bhat, H. S. Nagaraja, *Chem. Select.* **2020**, *5*, 2455.
[42] L. Yu, L. Wu, B. McElhenny, S. Song, D. Luo, F. Zhang, Y. Yu, S. Chen, Z. Ren, *Energy Environ. Sci.* **2020**, *13*, 3439.
[43] E. Gioria, S. Li, A. Mazheika, R. N. D'Alnoncourt, A. Thomas, F. Rosowski, *Angew. Chem., Int. Ed.* **2023**, *62*, e202217888.
[44] M. A. Ahsan, A. R. P. Santiago, Y. Hong, N. Zhang, M. Cano, E. Rodriguez-Castellon, L. Echegoyen, S. T. Sreenivasan, J. C. Noveron, *J. Am. Chem. Soc.* **2020**, *142*, 14688.
[45] H. Yen, Y. Seo, S. Kaliaguine, F. Kleitz, *ACS Catal.* **2015**, *5*, 5505.
[46] D. He, X. Song, W. Li, C. Tang, J. Liu, Z. Ke, C. Jiang, X. Xiao, *Angew. Chem., Int. Ed.* **2020**, *59*, 6929.
[47] M. Harilal, B. Vidyadharan, I. I. Misnon, G. M. Anilkumar, A. Lowe, J. Ismail, M. M. Yusoff, R. Jose, *ACS Appl. Mater. Interfaces* **2017**, *9*, 10730.
[48] F. Dietrich, J. Fernandez, S. Hevia, E. Cisternas, M. Flores, *J. Phys. Chem. C* **2021**, *125*, 20450.
[49] P. Thangavel, M. Ha, S. Kumaraguru, A. Meena, A. N. Singh, A. M. Harzandi, K. S. Kim, *Energy Environ. Sci.* **2020**, *13*, 3447.
[50] K. J. Carroll, J. U. Reveles, M. D. Shultz, S. N. Khanna, E. E. Carpenter, *J. Phys. Chem. C* **2011**, *115*, 2656.
[51] H. Zhang, D. Zhang, X. Lu, C. Liu, G. Zhou, X. Ma, L. Wang, P. Jiang, Q.-K. Xue, X. Bao, *Nat. Commun.* **2017**, *8*, 214.
[52] N. K. Oh, J. Seo, S. Lee, H.-J. Kim, U. Kim, J. Lee, Y.-K. Han, H. Park, *Nat. Commun.* **2021**, *12*, 4606.
[53] J. Liu, M. Li, S. Lustig, S. Lee, M. Flytzani-Stephanopoulos, *Appl. Catal. B: Environ.* **2018**, *226*, 234.
[54] R. J. Woolley, B. N. Illy, M. P. Ryan, S. J. Skinner, *J. Mater. Chem.* **2011**, *21*, 18592.
[55] M. Heilmann, C. Prinz, R. Bienert, R. Wendt, B. Kunkel, J. Radnik, A. Hoell, S. Wohlrab, A. G. Buzanich, F. Emmerling, *Adv. Eng. Mater.* **2022**, *24*, 2101308.
[56] H.-Y. Wang, S.-F. Hung, H.-Y. Chen, T.-S. Chan, H. M. Chen, B. Liu, *J. Am. Chem. Soc.* **2016**, *138*, 36.
[57] D. Gajdek, P. A. T. Olsson, S. Blomberg, J. Gustafson, P.-A. Carlsson, D. Haase, E. Lundgren, L. R. Merte, *J. Phys. Chem. C* **2022**, *126*, 3411.
[58] H. Shi, X. Dai, Q. Liu, T. Zhang, Y. Zhang, Y. Shi, T. Wang, *Ind. Eng. Chem. Res.* **2021**, *60*, 16011.
[59] A. G. Boudjahem, S. Monteverdi, M. Mercy, M. M. Bettahar, *Langmuir* **2004**, *20*, 208.
[60] M. B. Gawande, A. Goswami, F.-X. Felpin, T. Asefa, X. Huang, R. Silva, X. Zou, R. Zboril, R. S. Varma, *Chem. Rev.* **2016**, *116*, 3722.
[61] P. Qu, S. Yang, C. Wang, H. Han, *ACS. Omega* **2022**, *7*, 8840.
[62] Y. Ren, Y. Bai, G. Wang, Y. Liu, C. Mou, J. Chen, B. Wei, H. Wang, Y. Sun, *Energy Fuels* **2023**, *37*, 9289.
[63] X. Zhang, S. Ju, C. Li, J. Hao, Y. Sun, X. Hu, W. Chen, J. Chen, L. He, G. Xia, F. Fang, D. Sun, X. Yu, *Nat. Commun.* **2024**, *15*, 2815.
[64] A. Amiri, V. Yurkiv, A. H. Phakatkar, T. Shokuhfar, R. Shahbazian-Yassar, *Adv. Funct. Mater.* **2024**, *34*, 2304685.
[65] Y. Liang, Y. Zeng, X. Tang, W. Xia, B. Song, F. Yao, Y. Yang, Y. Chen, C. Peng, C. Zhou, C. Lai, *J. Chem. Eng.* **2023**, *451*, 138936.
[66] S. Mandal, N. Pandey, S. Singh, A. Ranjan, U. Ojha, *Mater. Chem. Front.* **2019**, *3*, 690.
[67] L. Xiao, S. Mou, W. Dai, W. Yang, Q. Cheng, S. Liu, F. Dong, *Angew. Chem., Int. Ed.* **2024**, *63*, e202319135.
[68] M. A. Mahmoud, R. Narayanan, M. A. El-Sayed, *Acc. Chem. Res.* **2013**, *46*, 1795.
[69] C. Rao, H. Wang, K. Chen, H. Chen, S. Ci, Q. Xu, Z. Wen, *Small* **2024**, *20*, 2303300.
[70] J. Li, R. Wei, X. Wang, Y. Zuo, X. Han, J. Arbiol, J. Llorca, Y. Yang, A. Cabot, C. Cui, *Angew. Chem., Int. Ed.* **2020**, *59*, 20826.
[71] B. Zhu, B. Dong, F. Wang, Q. Yang, Y. He, C. Zhang, P. Jin, L. Feng, *Nat. Commun.* **2023**, *14*, 1686.
[72] Q. Liang, G. Brocks, A. Bieberle-Hütter, *J. Phys. Energy* **2021**, *3*, 026001.
[73] S. A. Aashi, A. G. Krishankant, C. Bera, V. Bagchi, *Sustain. Energy Fuels* **2023**, *7*, 3692.
[74] G. Li, J. Yu, W. Yu, L. Yang, X. Zhang, X. Liu, H. Liu, W. Zhou, *Small* **2020**, *16*, 2001980.
[75] Q. Li, X. Wang, K. Tang, M. Wang, C. Wang, C. Yan, *ACS Nano* **2017**, *11*, 12230.
[76] Y. Qi, Y. Zhang, L. Yang, Y. Zhao, Y. Zhu, H. Jiang, C. Li, *Nat. Commun.* **2022**, *13*, 4602.